

# Characterization of the Mechanical Behavior of Colorado Mason Sand at Grain-Level by Nanoindentation

T. Xu<sup>1</sup> · Y. Du<sup>1</sup> · H. Luo<sup>1</sup> · Z. Hu<sup>1</sup> · X. Wang<sup>1</sup> · L. Guo<sup>1,2</sup> · H. Lu<sup>1</sup>

Received: 28 August 2017 / Accepted: 26 October 2017 / Published online: 27 November 2017  
© Society for Experimental Mechanics 2017

**Abstract** Colorado Mason sand has received increasing attention for use as a model granular material for the investigation of the soil response under a blast. The grain-level mechanical properties of Colorado Mason sand, which are important input for modeling and simulation of such granular material, are measured by nanoindentation. The as-received assorted sand is sorted into six grain sizes: 0.15 mm, 0.21 mm, 0.3 mm, 0.42 mm, 0.6 mm, and 0.84 mm. The sand chemical constituents are determined using energy dispersive X-ray spectroscopy, and three main types of sand grains are determined as silica, rock, and metal oxide. The Young's modulus and hardness are measured using nanoindentation with a Berkovich tip. A cube-corner indenter tip is used to generate radial cracks, the lengths of which are used to determine the fracture toughness. The mechanical properties (Young's modulus, hardness and fracture toughness) of the sand are statistically analyzed, and are found to follow a tri-modal Weibull distribution, corresponding to three main types of constituent grains. The grains show ductile behavior under Berkovich tip due to confinement by high pressure induced by the tip. An inverse method is used to determine the stress-strain relationship for individual sand grains using finite element analysis, with the consideration of Drucker-Prager yield criterion. The grain-level mechanical properties determined in this study can be used in microscale and mesoscale simulations.

**Keywords** Colorado Mason sand · Nanoindentation · Young's modulus · Hardness · Fracture toughness · Finite element method

## Introduction

Sand is a granular material consisting of an aggregate of particles with irregular geometry and surface topography. It exhibits complex mechanical behavior, and is unique in that it behaves in many aspects similar to other matters, such as solids, liquids, and gases. Due to its unique mechanical behavior, sand has numerous civil and military applications. It is used as an ingredient in concrete, a filler for sand bags, or simply used in its loose form. As such, sand is used in the construction of civil engineering structures and highways, in protection against floods or soil erosion, in ballistic protection for military structures. Sand is also used in manufacturing applications such as waterjet cutting, sand blasting, and sandcasting. Considerable research has been conducted to investigate the mechanical behavior of sand under quasi-static loading conditions [1–3]. Triaxial compression of sand was conducted to investigate the anisotropic behavior, softening behavior, and shear band formation [4–7]. The mechanical behavior of sand has also been characterized at high strain rates [8–10], and the effects of initial mass density, particle sizes, and moisture are investigated.

Investigation of the mechanical behavior of sand, from granular level to mesoscale and macro scale, can contribute towards a fundamental understanding of the underlying mechanisms of deformation, flow, and fracture of granular materials under load. It can ultimately be used to explain the large scale phenomena such as landslide and penetration [11–13]. For modeling those mechanisms mentioned above, numerical simulations using the finite element method (FEM), discrete

---

✉ H. Lu  
hongbing.lu@utdallas.edu

<sup>1</sup> Department of Mechanical Engineering, The University of Texas at Dallas, Richardson, TX 75080, USA

<sup>2</sup> Department of Civil Engineering, Yancheng Institute of Technology, Yancheng 224051, People's Republic of China

element method (DEM), peridynamics, and material point method (MPM) [14–23] are usually performed to capture the effects of solid/fluid interactions, surface roughness, irregular shape and anisotropy on the mechanical behavior [24]. The overall behavior of sand at mesoscale depends strongly on the grain-level mechanical behavior. Therefore, it is particularly important to determine the fundamental mechanical properties, such as Young's modulus, hardness, fracture toughness, and stress-strain relationship, of individual sand grains to provide accurate information for the numerical simulations of granular materials. However, due to the small size of sand grains, typically in the range of 0.1 to 1.5 mm with irregular shape, it is difficult to conduct conventional experiments, such as tension [25], compression [5, 26], shear [6, 27], and stress wave propagation [8, 9, 28], which are usually conducted for characterization of the mechanical properties of a material in bulk form. An effective technique, which overcomes the difficulty, is thus necessary to measure the mechanical properties of individual sand grains.

In recent years, instrumented nanoindentation technique, also known as depth-sensing indentation, has become an effective technique for determining the local mechanical properties at the microscale and nanoscale. Nanoindentation has been widely used to characterize the mechanical behavior of different types of materials, such as elastic-plastic [29], viscoelastic [30–32], and viscoplastic [33, 34] materials. Methods for measuring the elastic-plastic properties, such as Young's modulus and hardness, have been well established by Oliver and Pharr [35, 36]. This method has been implemented in commercially available nanoindenters, and has been applied to characterize the mechanical behavior of granular materials. Daphalapurkar et al. [37] investigated the grain-level mechanical behavior of Stillwater sand using nanoindentation, and determined its Young's modulus, hardness, fracture toughness and stress-strain relationship. Recently, Wang et al. [38] measured the mechanical properties such as modulus, hardness and fracture toughness of individual Eglin sand by nanoindentation, and reported that those properties follow the Weibull distribution. To determine the stress-strain relationship of sand grains, the von Mises yield criterion was used along with isotropic hardening to simulate the nanoindentation on sand grain [37, 38].

Recently, Colorado Mason sand has been used as the material for the investigation of soil blast and modeling [18–20, 22, 39–46]. However, the mechanical properties at granular level are not yet available. In this paper, nanoindentation is conducted to determine the mechanical properties of six sizes of Colorado Mason sand grains, sorted from the as-received poorly graded sand using shaking sieves. The energy dispersive X-ray spectroscopy (EDS) is used to determine the chemical constituents. Nanoindentation is made on two perpendicular surfaces of the same sand grain to examine the isotropy. For each size of sand grains, more than 150 nanoindentation experiments are conducted using a Berkovich tip. The

Young's modulus and the hardness are determined by analyzing the nanoindentation load-displacement curves. To measure the fracture toughness, a cube-corner indenter tip is used to induce cracks in the sand grain. A statistical method is used to analyze the nanoindentation experimental results. Finally, the stress-strain relationships are extracted by adopting an inverse method by way of finite element method (FEM) simulations. This paper is organized as follows: in the next section, specimen preparation is described, followed by explanation of the nanoindentation experimental setup and data analysis method. The results and discussions are then reported, and conclusions made are stated.

## Experiment and Simulation

### Sample Preparation

A poorly graded Colorado Mason sand, obtained from Colorado Materials in Longmont, Colorado, USA, is used in this study. In order to determine the chemical compound of the Colorado Mason sand, energy-dispersive X-ray spectroscopy (EDS) analysis is conducted under Zeiss Supra-40 scanning electron microscopic (SEM) system. The EDS spectra and corresponding SEM images are shown in Fig. 1. It is identified that Colorado Mason sand consists mainly of three types of materials [47]: (1) transparent sand grains that contain only Si and O, they are pure  $\text{SiO}_2$ , or silica sand grain; (2) Translucent sand grains that contain only Si, O, Al and Na, these are contaminated grains, they are called rock herein; (3) black sand grains that contain Fe and O, they are metal oxide grains. Colorado Mason sand is a local naturally occurring sand

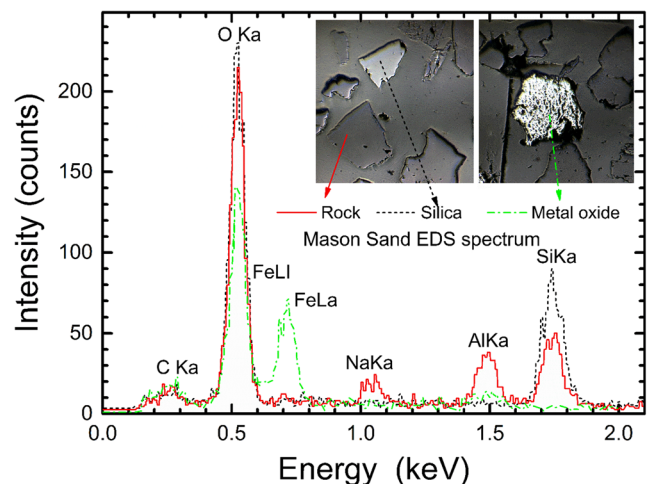


**Fig. 1** EDS spectra and SEM images of the polished Colorado Mason sand surface. In the left inset, the transparent sand grain (black arrow) is silica sand, and the corresponding EDS spectrum is shown as the black curve; the translucent sand grain (red arrow) is rock, and the corresponding EDS spectrum is shown as the red curve; the grain in the right inset is metal oxide, and its EDS spectrum is shown as the green curve

which includes the other two non-silica constituents, specifically rock and metal oxide. It is noted that silica grains can be colorless or white. The white particles are highly weathered and porous [41]. In this paper, the nanoindentation on silica grains is made on transparent particles only.

The as-received Colorado Mason sand is washed and subsequently dried in an oven at 55 °C for 24 h. A multi-directional shaker is used to sort out the sand grains [8, 37, 38]. The shaker (D-4326, DUAL Manufacturing Co, Franklin Park, IL) used a series of metal wire sieves following the ASTM standard E-11-09e1 (Specification for Wire Cloth and Sieves for Testing Purposes). To separate different sizes of the sand, the sand agglomerate is vibrated through a series of sieves stacked together, with the larger open-hole sizes at the top and gradually reducing to the smaller ones at the bottom. Following the ASTM standard D2487, the sand grains are sorted into grain sizes of 0.84 mm, 0.6 mm, 0.42 mm, 0.3 mm, 0.21 mm, and 0.15 mm through shaking sand grains on a set of stacked sieves of #20, #30, #40, #50, #70, and #100, respectively.

Samples for nanoindentation are prepared as follows. The sorted Colorado Mason sand grains are embedded in a cement matrix. Colorado Mason sand grains, cement, and water with a weight proportion of 10:30:9 are mixed and mounted in a sample holder. After curing for 36 h, the sand specimens are polished by a MultiPrep™ system polishing machine using alumina abrasive slurry with particle size from 1 μm to 50 nm. After polishing, the sand sample surfaces are cleaned by acetone followed by alcohol. Figure 2(a) shows an optical micrograph of the polished sand surface with several grains. Within the sand grains, defects such as small pits and ridges are observed, indicating the presence of defects inside the sand grains. An atomic force microscope (AFM) image of the polished sand surface profile is shown in Fig. 2(b). It is determined that the surface roughness root mean square (RMS) is approximately 2 nm, which is smooth enough for nanoindentation.

### Measurements of Young's Modulus and Hardness

An Agilent G200 nanoindenter is used for nanoindentation measurements. The nanoindentation system can reach a maximum indentation depth of 500 μm (resolution of 0.2 nm) and a maximum load of 500 mN (resolution of 50 nN). A Berkovich indenter tip, made from a single crystal diamond, is used to measure the Young's modulus and hardness. Nanoindentation is made on flat, polished sand grain surfaces under a constant loading rate of 2 mN/s. Nanoindentation sites are near the center of a sand grain, to minimize the edge effect. The applied load on the indenter tip is increased until it reaches 30 mN, followed by unloading. The nanoindentation load-displacement curve obtained is thus characteristic of that particular sand grain. Analysis is carried out to determine the mechanical properties of sand grains based on the contact

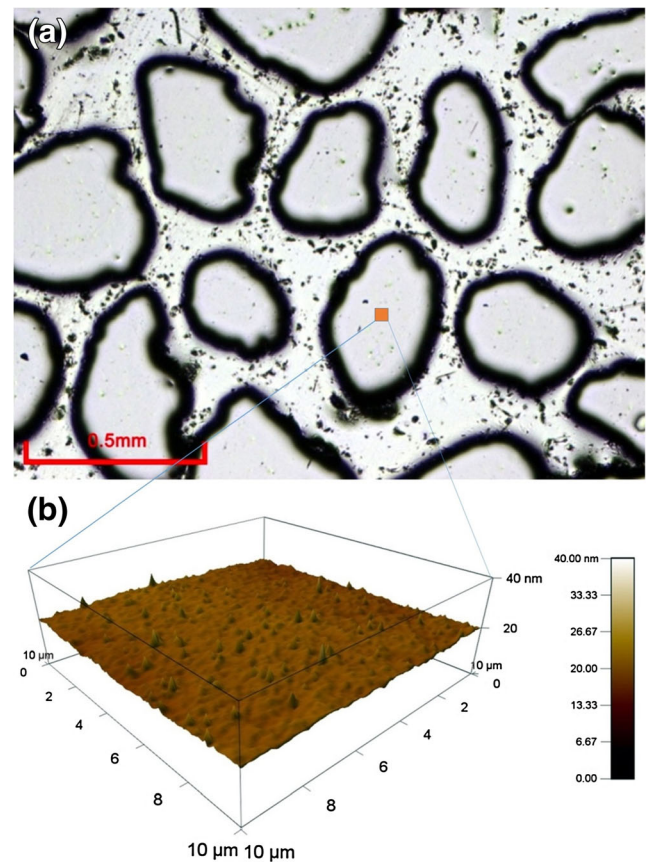


**Fig. 2** Surface images of a polished Mason sand surface: (a) optical micrograph of polished sand grains embedded in cement matrix, (b) Atomic force microscopy (AFM) image showing the surface topography of a sand grain after polishing. Surface roughness (RMS) is 2 nm

mechanics analysis of nanoindentation load-displacement relationships, which has been well established by Oliver and Pharr [35, 36].

The hardness ( $H$ ) is obtained using  $H = P_{\max}/A_c$ , where  $P_{\max}$  is the maximum nanoindentation load,  $A_c$  is the contact area corresponding to the contact depth ( $h_c$ ) at the maximum load, which is calculated based on the tip area function.

The reduced modulus  $E_r$  is obtained by  $1/E_r = (1 - \nu_s^2)/E_s + (1 - \nu_i^2)/E_i$ , where  $E_s$  and  $\nu_s$  are the Young's modulus and Poisson's ratio of the specimen, respectively, while  $E_i$  and  $\nu_i$  are the Young's modulus and Poisson's ratio of the diamond Berkovich indenter tip, respectively. Due to the finite stiffness of the indenter tip, its modulus is considered in the calculation of Colorado Mason sand grain modulus from the contact stiffness. The contact stiffness  $S$  is calculated from the slope of the initial unloading curve

$$S = \frac{dP}{dh} = \beta \frac{2}{\sqrt{\pi}} E_r \sqrt{A_c(h_c)} \quad (1)$$

where  $\beta$  is the indenter shape factor [36]. Equation (1) along with the known values of the area function, slope of the



unloading curve, and Young's modulus and Poisson's ratio of the Berkovich indenter tip are used to determine the Young's modulus of Colorado Mason sand grain. The hardness is calculated from the maximum load and the corresponding contact area. These are the direct outputs from the nanoindentation software, based on the Oliver-Pharr method [35, 36].

### Measurement of Fracture Toughness

When a brittle material is pressed by a sharp indenter tip under a sufficiently high load, three radial cracks are formed, and emanate from the indenter corners. In such a case, the fracture toughness can be determined by measuring the lengths of the radial cracks produced under a given nanoindentation load. In this investigation, a cubic-corner indenter tip, made of a single crystal diamond, is used to indent into a polished Colorado Mason sand grain to initiate cracks at the three corners of the tip. The average of the lengths of the three radial cracks produced under a given nanoindentation load is used to calculate the mode-I fracture toughness  $K_C$  using [48]

$$K_C = \alpha \left( \frac{E}{H} \right)^{0.5} \left( \frac{P_{\max}}{c^{3/2}} \right) \quad (2)$$

where  $\alpha$  is an empirical constant which takes into account of the geometry of the indenter tip (for a cubic-corner tip,  $\alpha = 0.032$ ),  $P_{\max}$  is the maximum load, and  $c$  is the crack length.  $E$  and  $H$  are the Young's modulus and hardness of the Colorado Mason sand grain, respectively.

### FEM Simulations to Determine the Stress-Strain Relationship

For determining the stress-strain relationship of Colorado Mason sand grains, nanoindentation is modeled using FEM. To determine the elastic-plastic properties of Stillwater and Eglin sand grains, the von Mises yield criterion has been used along with isotropic hardening to simulate the nanoindentation [37, 38]. However, the Drucker-Prager model is more widely used in mesoscale simulations to predict the mechanical behavior of the granular materials under impact loading [49–52]. Thus, in this paper, the Drucker-Prager yield criterion [49] is used to simulate the pressure-dependent yield behavior of Colorado Mason sand grains. The constitutive behavior of Colorado Mason sand grains under uniaxial compression is assumed to follow a linearly elastic, and power-law hardening plastic relationship, as shown below

$$\begin{cases} \varepsilon = \frac{\sigma}{E} & \text{for } \sigma \leq \sigma_0 \\ \varepsilon = \left( \frac{\sigma - \sigma_0}{K} \right)^{\frac{1}{n}} & \text{for } \sigma \geq \sigma_0 \end{cases} \quad (3)$$

where  $E$  is the Young's modulus,  $\sigma_0$  is initial compressive yield strength,  $n$  is the work hardening exponent, and  $K$  is the reference stress value. To ensure continuity, we have  $K = \sigma_0(E/\sigma_0)^n$ . The Drucker-Prager yield criteria is written as

$$\phi = \sqrt{3J_2} - \frac{I_1}{3} \tan \beta - \left( 1 - \frac{1}{3} \tan \beta \right) \sigma_0 = 0 \quad (4)$$

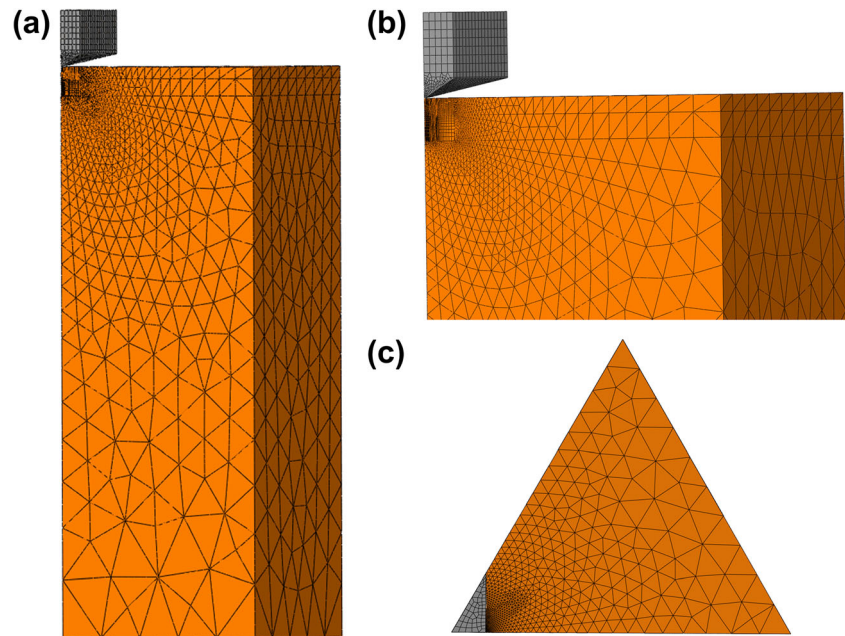
where  $\beta$  is the friction angle, and  $\sigma_0$  is the uniaxial compressive yield strength. In equation (4),  $\sigma_e = \sqrt{3J_2}$  and  $\sigma_m = I_1/3$  are the von Mises stress and hydrostatic pressure, respectively.  $I_1$  is the first invariant of the Cauchy stress  $\sigma_{ij}$ , and  $J_2$  is the second invariant of the deviatoric part of the Cauchy stress

$$I_1 = \sigma_{ii}, s_{ij} = \sigma_{ij} - \frac{\sigma_{ii}}{3}, J_2 = \frac{1}{2} s_{ij} s_{ji} \quad (5)$$

The Young's modulus and hardness have been measured from nanoindentation experiment directly. An inverse method is used to determine the material properties of  $\sigma_0$ ,  $n$ , and  $\beta$  for Colorado Mason sand grains. To this end, FEM is used to simulate the nanoindentation. The commercial software package ABAQUS V6.14 is used for the modeling. A typical three-dimensional (3D) FEM model used to simulate the nanoindentation is shown in Fig. 3. Considering the three-fold symmetry of the pyramidal Berkovich indenter, only one sixth of the entire 3D model is used in simulations to reduce the computational time. The actual tip geometry of the Berkovich indenter used in this work, including the tip bluntness, is determined by conducting tip geometry calibration experiment on a standard fused silica sample. It is found that the Berkovich indenter used in this paper has a tip rounding radius of approximately 100 nm. The indenter bluntness is then taken into account in the FEM simulations. The height and width of the FEM model are selected to be 100 and 50  $\mu\text{m}$ , respectively. This model size is found to be large enough to avoid sample size effect on the nanoindentation load-displacement curve. The FEM model contains 48,600 linear hexahedral elements (C3D8R) and 117,973 quadratic tetrahedral elements (C3D10). Adaptive meshing is used with very fine mesh assigned in the region underneath the Berkovich indenter. Mesh convergence studies are conducted to ensure that proper mesh refinement has been achieved. The displacement history from the experiment is given as input for the FEM simulations. The Poisson's ratio is assumed to be 0.18, and the Young's modulus values determined by experiment are used as input for the FEM simulations. The output of the FEM simulation is the resulting nanoindentation load under the prescribed displacement. This numerical nanoindentation load is plotted as a function of the nanoindentation displacement, to generate the simulated load-displacement curve. The compressive yield strength  $\sigma_0$ , work hardening exponent  $n$ , and friction angle  $\beta$  are adjusted until a good agreement is



**Fig. 3** Finite element method (FEM) simulation model for nanoindentation on a 1/6th model for the Colorado Mason sand grain indented by a Berkovich tip: (a) side view of the overall geometry and the mesh, (b) side view at a higher magnification, (c) top view of the model



reached between the experimental and simulated nanoindentation load-displacement curves. The best-fit parameters are then used to determine the stress-strain relationship for the Colorado Mason sand grains.

It is noted that the plastic properties, determined by an inverse method using a single nanoindentation load-displacement curve does not yield unique solution in certain cases [53]. In our previous work on nanoindentation on Stillwater and Eglin sand grains [37, 38], the inverse method proposed by Shim et al. [54] was used to extract successfully the stress-strain curve of a single sand grain from FEM simulation. In this paper, however, the same inverse methodology is not directly applicable because of the implementation of Drucker-Prager yield criterion. For hydrostatic pressure-dependent yielding, Peng et al. [55] reported an the inverse method to determine the Drucker-Prager plastic properties using nanoindentation. From their dimensional analysis and FEM simulations, it was found that, for a material which has pressure-dependent yield behavior, nanoindentation on two materials with different sets of plastic properties cannot yield the same loading–unloading curve. A unique solution can be obtained from one nanoindentation load-displacement curve. Details are described in [55].

## Results and Discussion

### Grain Size Distribution

The curve for the percent finer by weight as a function of grain size is shown in Fig. 4. The six major sizes of sand grains are 0.84 mm, 0.6 mm, 0.42 mm, 0.3 mm, 0.21 mm, and 0.15 mm, respectively. The median grain size is determined as 0.42 mm.

The sieve opening size of  $d_{60}$  allows 60% of the sand by the weight to pass, determined as 0.5 mm. Similarly, the effective grain size for  $d_{10}$  is determined as 0.17 mm, and uniformity (defined as  $d_{60}/d_{10}$ ) is 2.94, indicating that there is a narrow size distribution for Colorado Mason sand grains.

### Young's Modulus and Hardness

For the measurement of Young's modulus and hardness, a Berkovich tip is used in nanoindentation on the Colorado Mason sand grain. Figure 5(a) shows the typical nanoindentation load-displacement curves for these three types of grains, specifically silica sand, rock, and metal oxide. Figure 5(b) shows a typical nanoindentation residual impression on silica sand grain using AFM, and Fig. 5(c) shows a typical inverted image. The inverted image (Fig. 5(c)) enables the determination of the nanoindentation depth and delineates its topographical features. It is seen that no cracks are formed by

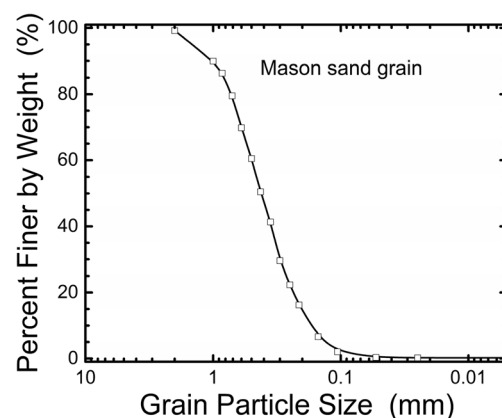


**Fig. 4** Particle size distribution curve for Colorado Mason sand grains

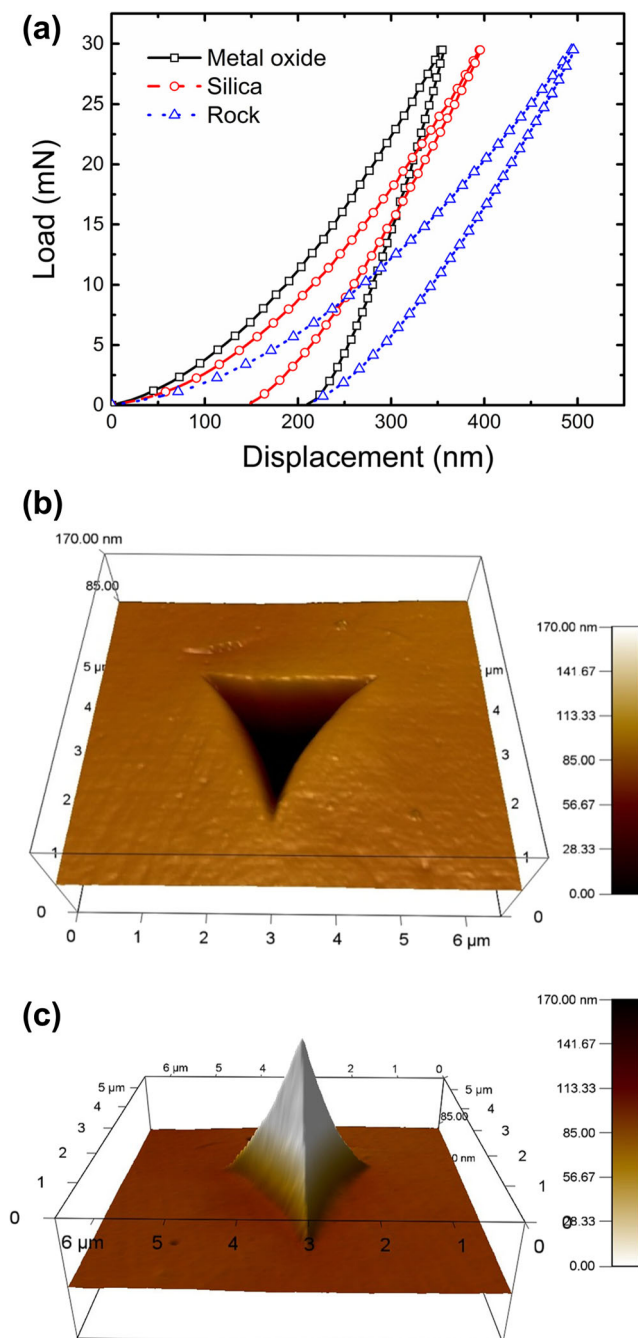


**Fig. 5** Typical nanoindentation experimental results: (a) typical nanoindentation load-displacement curves for Colorado Mason sand consists of silica grain, rock, and metal oxide, (b) residual indent impression profiled by AFM (c) 3D inverted image of the residual indent impression

in nanoindentation using Berkovich indenter tip. Thus, the continuum approximation is appropriate, and Oliver-Pharr method [35, 36] can be used to determine the Young's modulus and hardness of the Colorado Mason sand grains.

The method developed by Oliver and Pharr [35, 36], in general, is not suitable for materials with anisotropic properties [38]. To determine whether the Colorado Mason sand

grains are isotropic or not, nanoindentation experiments are conducted on the two perpendicular edge sections in a quarter of a Colorado Mason sand grain. If the indentation modulus is very close to each other on the two perpendicular surfaces, the grain can be treated isotropic in amorphous (non-crystalline) form or pseudo-isotropic in polycrystalline. A large sand grain (0.84 mm) is chosen and embedded in a cement matrix to form an approximately 4.1 mm thick disk, the disk is subsequently cut into a rectangular bar (20 mm in length, and 8.1 mm in width), as shown in Fig. 6. The polishing procedure mentioned earlier is used to generate smooth surfaces. Nanoindentation is made on a transparent silica grain and a red opaque rock grain. For nanoindentation made on the two perpendicular surfaces, the Young's modulus is calculated by Oliver-Pharr method. For the rock grain, the Young's modulus values for two perpendicular sides are  $84.8 \pm 10.2$  GPa and  $88.1 \pm 5.0$  GPa, respectively. Young's modulus values for two perpendicular surfaces of silica grain are  $108.7 \pm 1.5$  GPa and  $103 \pm 1.6$  GPa, respectively. Young's modulus values for the two perpendicular surfaces are in general very close to each other, indicating that the Colorado Mason sand grain can be modeled as an isotropic material. The slight difference is likely due to the fact that the two actual edges are not perfectly perpendicular to the indenter axis because of the manual preparation of the sample.

In order to investigate the size-dependence of the mechanical properties of Colorado Mason sand, for each sorted sand specimen, nanoindentation is made on 150 different grains with one nanoindentation per grain. Each nanoindentation location is chosen in an area with a smooth polished surface. The nanoindentation sites are near the center of a sand grain, to avoid potential edge effect. Nanoindentation load-displacement curves are analyzed, subsequently the Young's modulus and hardness are determined. The Young's modulus values for grain sizes of 0.15 mm, 0.21 mm, 0.3 mm, 0.42 mm, 0.6 mm, and 0.84 mm are determined as  $97.7 \pm 35.4$  GPa,  $108.1 \pm 42.2$  GPa,  $92.9 \pm 40.6$  GPa,  $93.9 \pm 21.7$  GPa,  $100.7 \pm 30.1$  GPa, and  $105.4 \pm 31.5$  GPa,

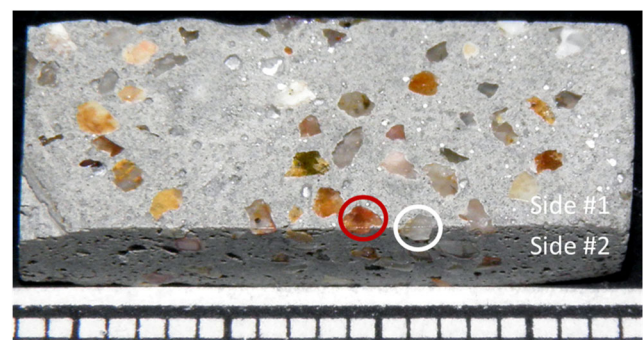


**Fig. 6** Rectangular bar sample for Colorado Mason sand grains used for examination of properties on different surface orientations using nanoindentation. The red circle indicates a rock grain and the white circle marks a silica grain. The grid is scale bar in 1 mm unit

respectively. The corresponding hardness values are  $11.1 \pm 4.2$  GPa,  $12.8 \pm 2.5$  GPa,  $10.0 \pm 4.8$  GPa,  $11.5 \pm 3.7$  GPa,  $12.7 \pm 3.2$  GPa, and  $12.5 \pm 3.7$  GPa, respectively. Scatter in the data is attributed to different types of sand grains, specifically silica, rock and metal oxide. These results indicate that size effect is not strong for both Young's modulus and hardness.

### Statistical Analysis of Young's Modulus and Hardness

The Weibull distribution is widely used to describe the distribution of the mechanical properties for materials with defects [56]. It has been used to describe the particle size distribution before and after impact of Eglin sand [9], and mechanical properties of Eglin sand, including Young's modulus,

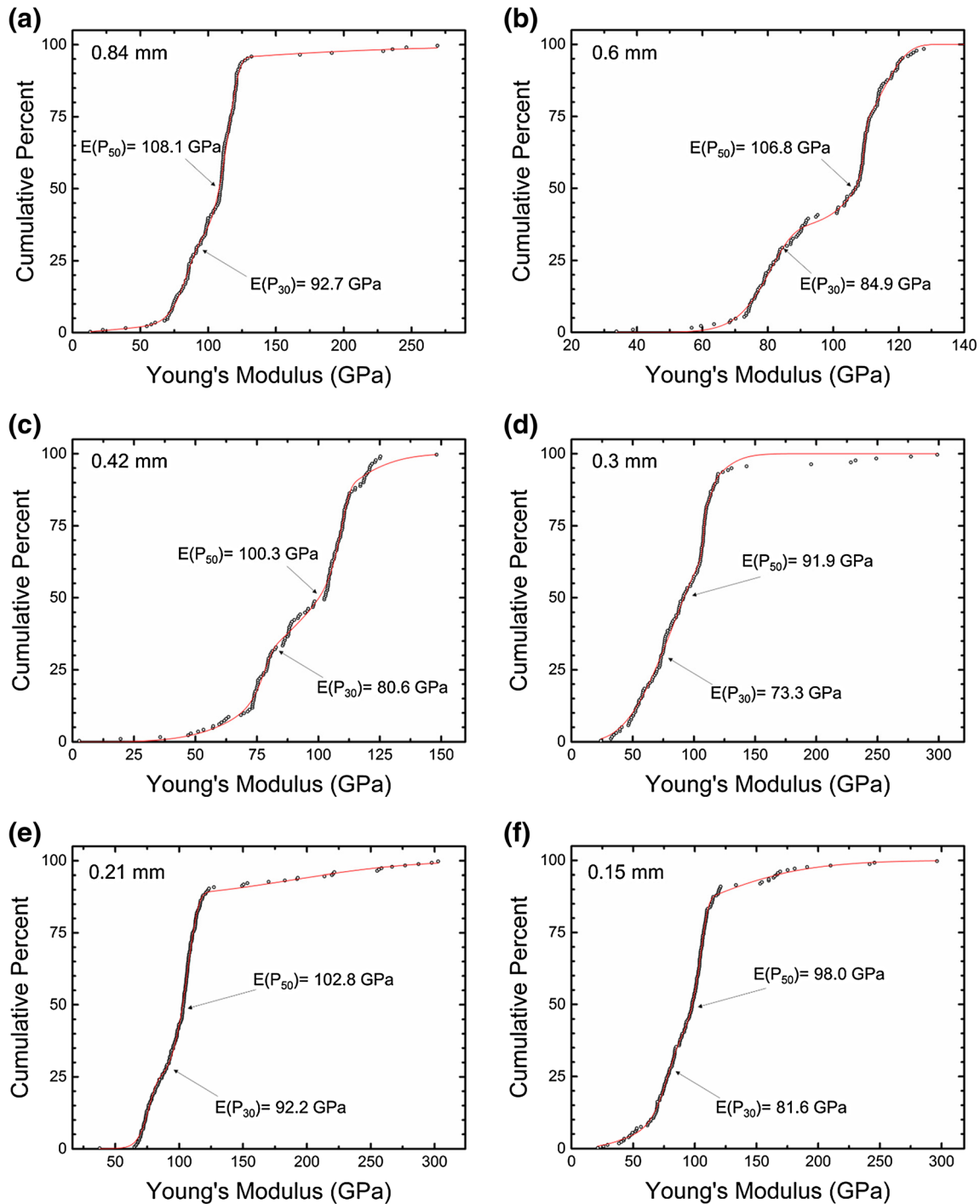


**Fig. 7** The Weibull plots of Young's modulus data from nanoindentation on six different sizes of sand grains: (a) 0.84 mm, (b) 0.6 mm, (c) 0.42 mm, (d) 0.3 mm, (e) 0.21 mm, (f) 0.15 mm. The black circles are experimental data, and the red solid lines are tri-modal Weibull cumulative distribution function (CDF)



hardness, and fracture toughness measured by nanoindentation [38]. It is found that the Weibull distribution can describe the statistical information better than the Gaussian distribution [9]. The Weibull cumulative distribution function (CDF) is given as

$$F(x) = 1 - e^{-(x/\lambda)^k}, x \geq 0 \quad (6)$$

where  $k > 0$  is the shape parameter and  $\lambda > 0$  is the scale parameter of the distribution; and  $F(x) = 0$  for  $x < 0$ . The Weibull distributions of the Young's modulus and the hardness values are plotted in Figs. 7 and 8, respectively. It is found that both the Young's modulus and the hardness do not follow a single Weibull distribution (equation (6)), rather, it follows a multi-modal Weibull distribution. If the results follow a single-modal Weibull distribution, the data shall follow a straight line

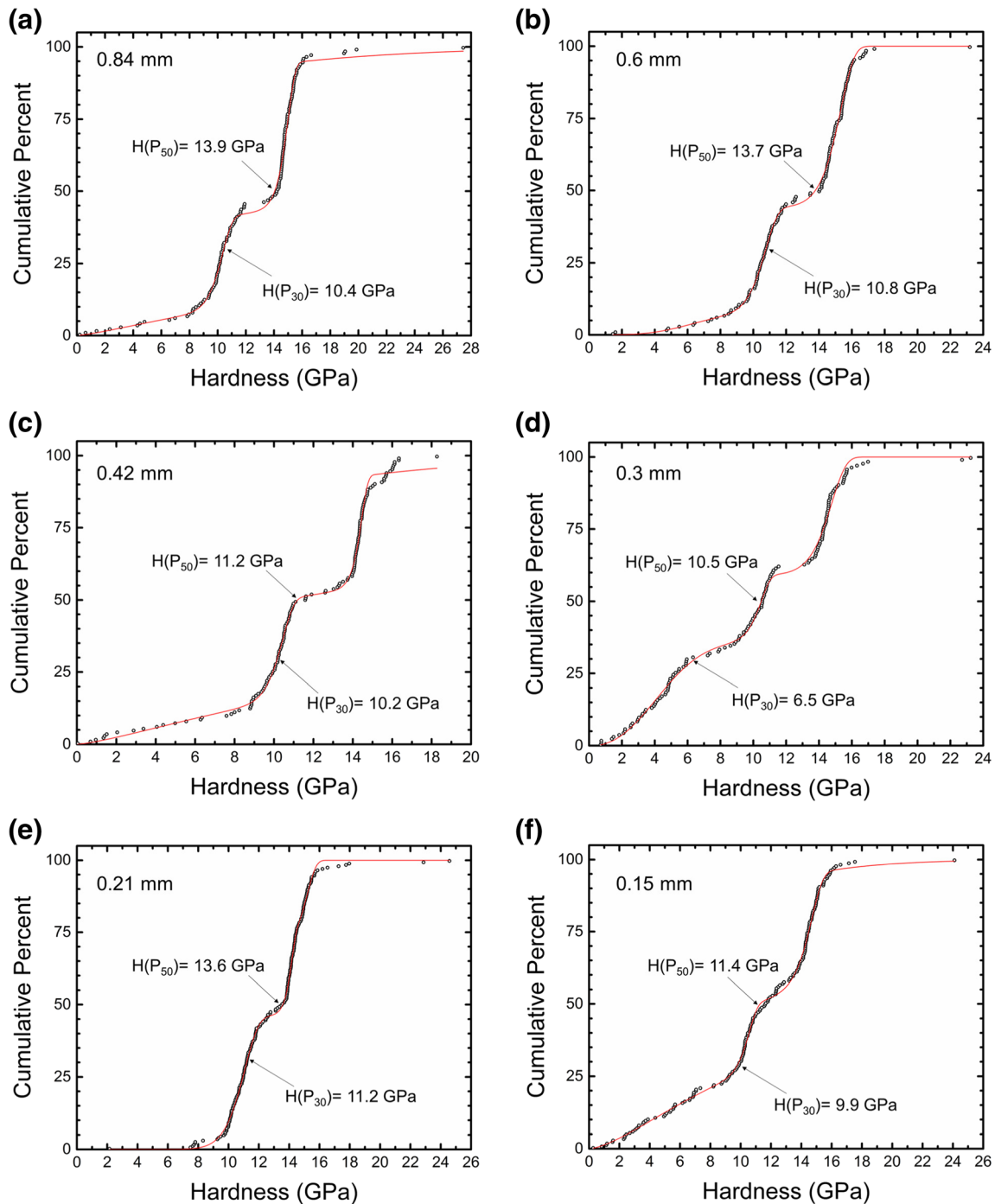


**Fig. 8** The Weibull plots of hardness from nanoindentation on six different sizes of sand grains: (a) 0.84 mm, (b) 0.6 mm, (c) 0.42 mm, (d) 0.3 mm, (e) 0.21 mm, (f) 0.15 mm. The black circles are experimental data, and the red solid lines are tri-modal Weibull CDF



**Table 1** Properties and parameters of the Weibull distribution for Young's modulus of Colorado Mason sand

Sand grain size		0.84 mm	0.6 mm	0.42 mm	0.3 mm	0.21 mm	0.15 mm	All sizes
Young's modulus E (GPa)	P <sub>50</sub>	108.1	106.8	100.3	91.9	102.8	98.0	101.9
	P <sub>30</sub>	92.7	84.9	80.6	73.3	92.2	81.6	84.1
Sample number		157	158	157	150	214	193	1029
Weibull shape $k_1$		10.5	12.8	23.6	4.19	14.4	9.5	10.2
Weibull shape $k_2$		15.5	131.6	4.27	3.39	14.1	18.7	17.1
Weibull shape $k_3$		1.32	14.7	34.0	50.1	3.01	1.96	1.99
Weibull scale $\lambda_1$		84.8	81.4	78.3	73.8	76.9	79.1	80.3
Weibull scale $\lambda_2$		115.5	109.6	101.2	102.7	107.6	105.3	109.8
Weibull scale $\lambda_3$		153.0	114.6	109.7	108.9	216.1	125.1	131.0
Weight factor $\varpi_1$		0.265	0.357	0.151	0.261	0.220	0.266	0.283
Weight factor $\varpi_2$		0.641	0.465	0.543	0.535	0.652	0.447	0.510
Weight factor $\varpi_3$		0.094	0.178	0.306	0.214	0.128	0.287	0.207

Weibull parameters with subscripts  $i = 1, 2, 3$  correspond to rock, silica, and metal oxide, respectively

in the Weibull probability plot. For the case of Colorado Mason sand grains, the data points follow an S-shape on the Weibull plot. It is likely due to the existence of three constituents, specifically silica grains, rock, and metal oxide, with each potentially following a distinct Weibull distribution. To take this into account, tri-modal Weibull distribution is used, and the CDF equation is modified as

$$F(x) = 1 - \sum_{i=1}^3 \varpi_i e^{-(x/\lambda_i)^{k_i}}, x \geq 0 \quad (7)$$

where  $k_i$  and  $\lambda_i$  ( $i = 1, 2, 3$ ) are the shape parameters and scale parameters, respectively.  $\varpi_i$  ( $i = 1, 2, 3$ ) are the three weight factors for three types of sand grains. The summation of the weight factors equals 1.

As shown in Figs. 7 and 8, the fitted tri-modal Weibull CDF curves agree reasonably well with the Young's modulus and hardness data. The actual median value (corresponding to P<sub>50</sub> value) for Young's modulus and hardness for the six sizes of sand grains are listed in Tables 1 and 2, respectively. The P<sub>30</sub> values (defined as 30% cumulative probability in equation (7)), often used in geosciences, are also provided in comparison with the P<sub>50</sub> values in Tables 1 and 2. The Weibull parameters for the six sizes of sand grains are also listed in Tables 1 and 2, for the Young's modulus and hardness, respectively. Scatter in the data is attributed to different types of sand grains due primarily to the variations in the material constituents, defects, and crystal orientations. A close examination indicates that when sand grain size changes from 0.84, 0.6, 0.42 to 0.3 mm, the P<sub>30</sub> Young's modulus values decrease from 92.7 GPa, 84.9 GPa, 80.6 GPa to 73.3 GPa, respectively.

**Table 2** Properties and parameters of the Weibull distribution for hardness of Colorado Mason sand

Sand grain size		0.84 mm	0.6 mm	0.42 mm	0.3 mm	0.21 mm	0.15 mm	All sizes
Hardness (GPa)	P <sub>50</sub>	13.9	13.7	11.2	10.5	13.6	11.4	12.7
	P <sub>30</sub>	10.4	10.8	10.2	6.5	11.2	9.9	10.4
Sample number		157	158	157	150	214	193	1029
Weibull shape $k_1$		15.7	3.71	19.6	2.39	13.3	1.49	16.9
Weibull shape $k_2$		1.27	15.2	1.33	19.2	48.8	20.7	1.38
Weibull shape $k_3$		29.5	19.8	46.0	17.9	27.5	20.9	22.3
Weibull scale $\lambda_1$		10.4	6.72	10.5	5.09	11.2	9.16	10.7
Weibull scale $\lambda_2$		13.4	10.8	11.7	10.5	14.2	10.6	10.8
Weibull scale $\lambda_3$		15.0	15.4	14.5	14.8	15.2	14.7	14.8
Weight factor $\varpi_1$		0.317	0.0705	0.347	0.362	0.300	0.375	0.297
Weight factor $\varpi_2$		0.180	0.369	0.266	0.229	0.459	0.226	0.263
Weight factor $\varpi_3$		0.503	0.560	0.387	0.409	0.241	0.399	0.440

Weibull parameters with subscripts  $i = 1, 2, 3$  correspond to rock, metal oxide, and silica, respectively



As the grain size decreases further, the  $P_{30}$  Young's modulus values become 92.2 GPa, and 81.6 GPa for grain sizes 0.21 mm, and 0.15 mm, respectively. The  $P_{50}$  Young's modulus values show the similar trend. The minimum Young's modulus is attained at sand size of 0.3 mm, which is the median grain size of the Colorado Mason sand. Similarly, for the hardness of the six grain sizes, the hardness value is found to reach its lowest at the median grain size of 0.3 mm. Combining the nanoindentation results of all Colorado Mason sand grains with all six sizes together, the tri-modal Weibull distributions for Young's modulus and hardness for assorted Colorado Mason sand are determined, as shown in Figs. 9(a) and (b), respectively. The Weibull parameters are also listed in Tables 1 and 2, with 95% confidence intervals for the assorted sand grains. The overall Young's modulus and hardness for the Colorado Mason sand grains are found to be 101.9 GPa

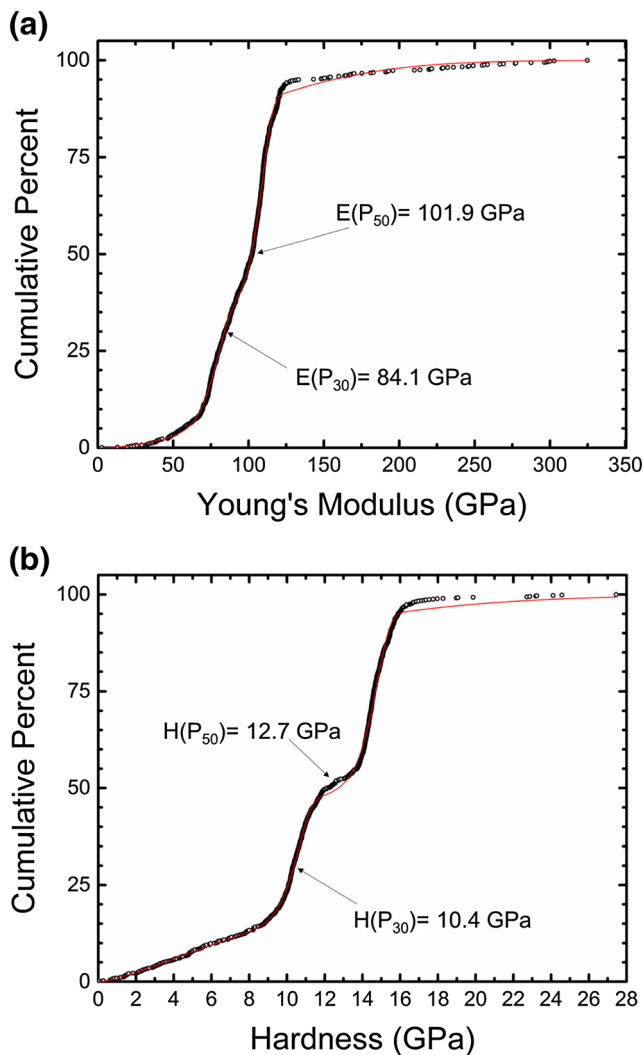


**Fig. 9** The Weibull plots of mechanical properties measured by nanoindentation for assorted Colorado Mason sand grains of all sizes: (a) Young's modulus, (b) hardness. The black circles are experimental data, and the red solid lines are tri-modal Weibull CDF

and 12.7 GPa, respectively. Within each size of sand grains, through comparison of the scale parameters range, silica sand, rock and metal oxide can be clearly distinguished from each other. For all sizes of sand, Young's modulus/hardness of silica sand, rock and metal oxide grain can be obtained from three scale parameters  $\lambda_i$  ( $i = 1, 2, 3$ ) as 109.8 GPa/14.8 GPa, 80.3 GPa/10.7 GPa, and 131 GPa/10.8 GPa, respectively. The weighting factors are averaged from the Young's modulus and hardness, and it is found that the mass ratio of three sand grains: rock, silica and metal oxide is 29:47.5:23.5.

### Fracture Toughness

A calibration experiment is conducted on a standard fused silica sample for evaluation of equation (2). The average value for fracture toughness obtained is  $0.60 \text{ MPa} \cdot \text{m}^{0.5}$ , which is in a reasonably good agreement with the value ( $0.58 \text{ MPa} \cdot \text{m}^{0.5}$ ) reported by Harding et al. [57].

For Colorado Mason sand, the values of the Young's modulus ( $E$ ) and hardness ( $H$ ) are obtained using Berkovich tip. This is followed by nanoindentation with a cube-corner tip. The average values for  $E$  and  $H$  are used to determine  $E/H$  for

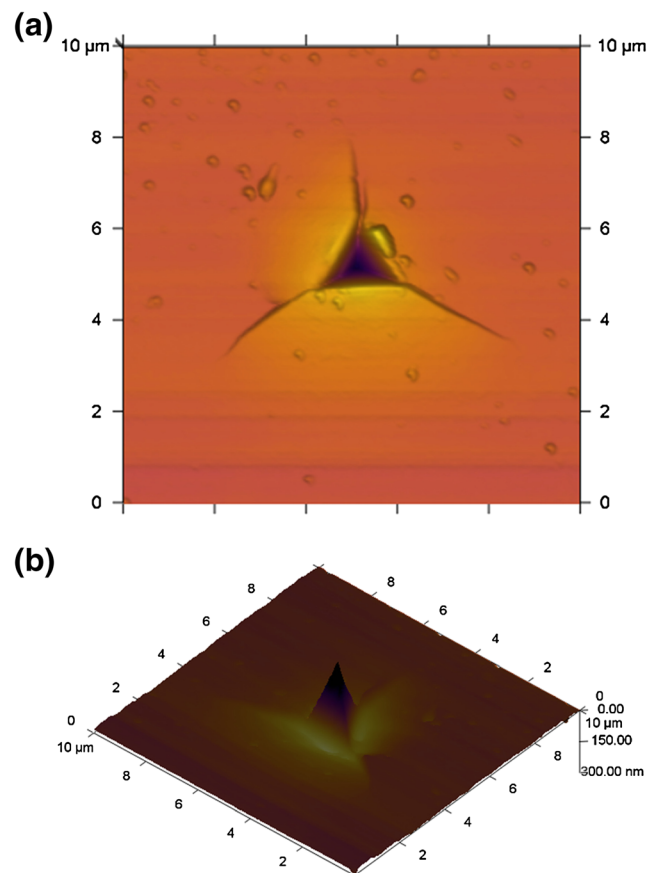


**Fig. 10** A typical nanoindentation crack surface profile under a cube corner tip at the maximum load of 40 mN: (a) 2D AFM surface image, (b) 3D inverted AFM image

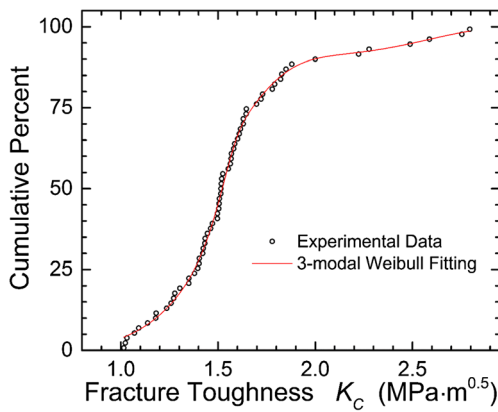


**Fig. 11** Weibull plot of fracture toughness from nanoindentation on six sizes in Colorado Mason sand grains

all sizes of sand grains. The  $E/H$  is determined as 8.0 for the assorted sand grains. In equation (2), the crack length  $c$  is determined from the surface topography by AFM. A typical topography is shown in Fig. 10(a). The same indent is also shown in 3D (inverted image) in Fig. 10(b). The cracks emanating from the three indenter corners are clearly seen. Due to potentially slight misalignment and instability of the crack propagation, the three cracks have different lengths. In calculation of the fracture toughness  $K_C$ , the average crack length is used. The tri-modal Weibull CDF plot for fracture toughness values obtained is shown in Fig. 11. The fracture toughness has a range from 1.02 to 2.80  $\text{MPa} \cdot \text{m}^{0.5}$ , the median value for the fracture toughness is determined as 1.52  $\text{MPa} \cdot \text{m}^{0.5}$ . The Weibull parameters are also listed in Table 3. It is found that cracks on some grains are not exactly straight, which is likely due to the inhomogeneity within a single sand grain, such as presence of defects [37]. Through comparison of the weight factor, the fracture toughness of silica sand, rock and metal oxide grain can be

**Table 3** Properties and parameters of the Weibull distribution for fracture toughness of Colorado Mason sand

Sand grain sizes		All sizes
Fracture toughness ( $\text{MPa} \cdot \text{m}^{0.5}$ )	$P_{50}$	1.52
	$P_{30}$	1.41
Sample number		65
Weibull shape $k_1$		10.0
Weibull shape $k_2$		21.7
Weibull shape $k_3$		6.16
Weibull shape $\lambda_1$		2.61
Weibull shape $\lambda_2$		1.53
Weibull shape $\lambda_3$		1.58
Weight factor $\varpi_1$		0.0963
Weight factor $\varpi_2$		0.253

Weibull parameters with subscripts  $i=1,2,3$  correspond to metal oxide, rock, and silica grains, respectively

obtained from three scale parameters  $\lambda_i$  ( $i=1, 2, 3$ ) as 1.58  $\text{MPa} \cdot \text{m}^{0.5}$ , 1.53  $\text{MPa} \cdot \text{m}^{0.5}$  and 2.61  $\text{MPa} \cdot \text{m}^{0.5}$ , respectively.

### FEM Simulation to Determine Stress-Strain Relationship

For determining the stress-strain relationship of granular sand material, nanoindentation is modeled using FEM. The  $P_{30}$  values in nanoindentation load-displacement curves are used for simulation. As stated earlier, the Berkovich indenter has a tip rounding radius of approximately 100 nm. The indenter bluntness is then taken into account in the FEM simulations. The Drucker-Prager yield criteria is used instead of von Mises yield criteria, due to the pressure-sensitive yield behavior of Colorado Mason sand. An inverse problem solving approach is used to determine the stress-strain relationship of sand at granular level by allowing the FEM simulated

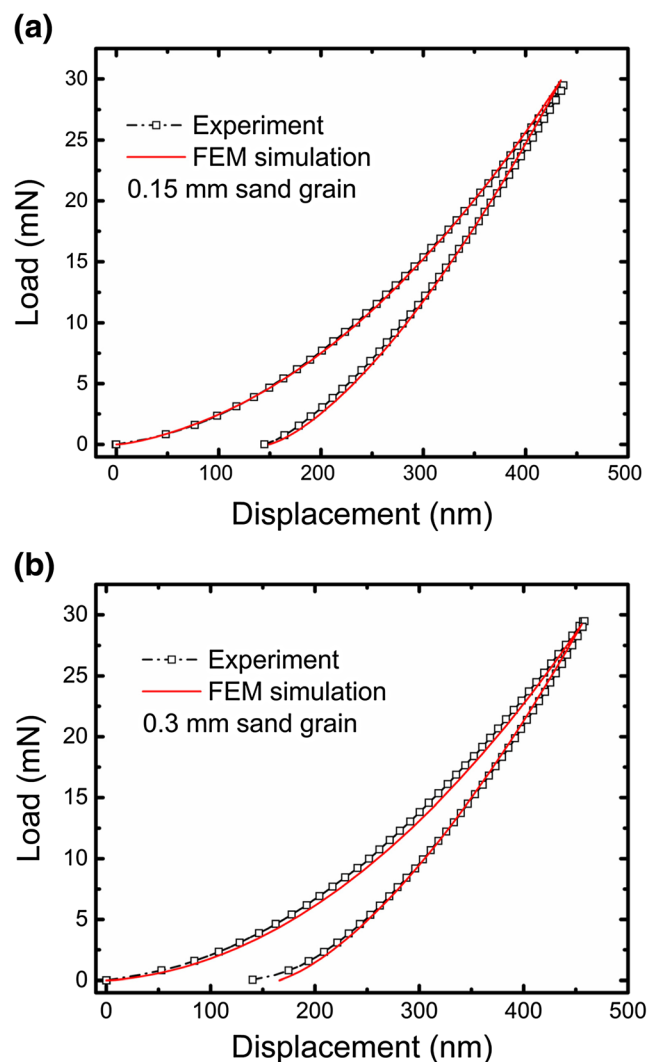
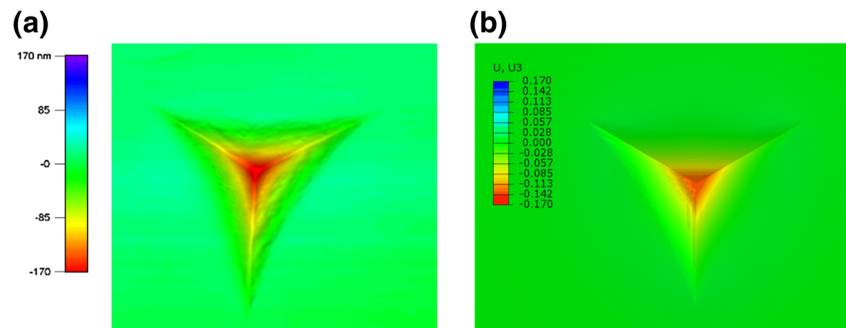


**Fig. 12** Comparison of experimental and FEM simulated load-displacement curves for: (a) 0.6 mm Colorado Mason sand grain, (b) 0.3 mm Colorado Mason sand grain

**Fig. 13** Comparison of FEM and AFM images of the out-of-plane displacement at a residual indent impression at nanoindentation depth of 170 nm: (a) AFM image (b) FEM result



nanoindentation load-displacement curve to agree with the experimental data. Figure 12 shows the FEM simulation results compared with the representative experimental data of  $P_{30}$ . In this case, two sand grain sizes, specifically, 0.15 mm and 0.3 mm, are shown as an example. They are in general agreed with each other reasonably well. Figures 13(a) and (b) show a comparison of the FEM simulated out-of-plane displacement plot and the AFM image of the indent after unloading the indenter. Even though it is somewhat difficult to precisely capture in the simulations all phenomena observed in experiments, both figures show similar features. It is observed that the simulated indent impression is in a reasonably good agreement with experimental data. The predicted stress-strain response is represented in the form of linearly elastic – power law hardening plastic model, and the compressive yield strength obtained for grain sizes of 0.15 mm, 0.21 mm, 0.3 mm, 0.42 mm, 0.6 mm, and 0.84 mm are determined as 3.0 GPa, 3.5 GPa, 2.9 GPa, 3.1 GPa, 3.3 GPa, and 3.3 GPa, respectively. The corresponding work hardening exponent  $n$  obtained for grain sizes are found to be 0.20, 0.18, 0.23, 0.22, 0.18, and 0.19 respectively. These parameters are summarized in Table 4. The friction angle for all sorted grain sizes is  $40.0^\circ$ .

In this study, the nanoindentation on silica, rock, and metal oxide grain is simulated for 0.84 mm Colorado Mason sand. The experimental load-displacement curves are selected such that the Young's modulus values for the grains are in the neighborhood of the Weibull scale parameters. The Young's modulus values determined from experiments, along with the displacement history, are used as input for FEM simulations. The plastic properties are modified until simulated data agreed with experimental load-displacement curves, as shown in Fig. 14. The calculated stress-strain response is represented in the form of linearly elastic – power law hardening plastic model, and the compressive yield strength obtained for rock,

silica, and metal oxide grain are determined as 1.4 GPa, 3.3 GPa, and 4.8 GPa, respectively. The corresponding work hardening exponent  $n$  values obtained are found to be 0.29, 0.19, and 0.2 respectively. The friction angles for rock and silica grain are  $40^\circ$ , while the friction angle for metal oxide grain is  $0^\circ$ . These parameters are summarized in Table 5. It is noted that, the hardening exponent of Colorado Mason sand can reach 0.2, which is typically observed for ductile material such as metals. Similar ductile behavior was also observed for both Stillwater and Eglin sand [37, 38]. As shown in Fig. 5(c), no cracks were observed in the 3D inverse image of the nanoindent under a Berkovich tip on Colorado Mason sand grain, and nanoindentation impression clearly shows ridges indicative of plastic deformation, associated with ductile flow in an otherwise conceived brittle grain. The highly ductile behavior under nanoindentation by a Berkovich tip is likely due to confinement provided by the high pressure induced by the Berkovich tip, the confinement pressure can reach 12.5 GPa levels.

It is noted that, for self-similar indenters, such as Berkovich and conical, load ( $P$ ) follows the following relationship with depth ( $h$ ), namely Kick's law [58],  $P = Ch^2$ , where  $C$  is a measure of the nanoindentation compliance, which depends on the elastic-plastic properties of the material, and the indenter geometry [59, 60]. A deviation of experimental loading-displacement curves from Kick's law has also been observed by other researchers, in certain situations due to one or more of the following effects [58, 61]: surface roughness, machine compliance and thermal drift [61]; rate-dependent deformation [61]; improper fitting [62]; indenter bluntness, at small nanoindentation depth, the tip rounding radius of the real Berkovich tip reduces the exponent  $n$  towards the value of 1.5 for sphere indenter [63–65]; indentation size effects [66–70]; and inhomogeneity.

**Table 4** Drucker-Prager parameters for different sizes of Colorado Mason sand grains

Sand grain size	0.84 mm	0.6 mm	0.42 mm	0.3 mm	0.21 mm	0.15 mm
$\sigma_0$ (GPa)	3.3	3.3	3.1	2.9	3.5	3.0
$n$	0.19	0.18	0.22	0.23	0.18	0.20
$\beta$ ( $^\circ$ )	40	40	40	40	40	40



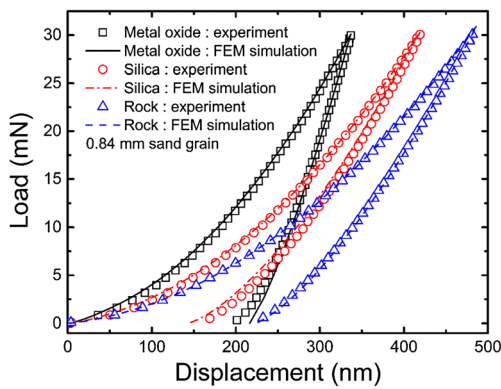


**Fig. 14** Comparison of nanoindentation experimental and FEM simulated load-displacement curves for 0.84 mm Colorado Mason sand grain with three types of constituent

For nanoindentation made on Colorado Mason sand grains, it is found that all the nanoindentation load-displacement curves of Colorado Mason sand grains do not follow the Kick's law. The exponent is about 1.8 instead of 2. In this investigation, well-polished samples with the surface roughness (RMS) about 2 nm are used, the machine compliance has been calibrated and thermal drift is below 0.05 nm/s. They are very unlikely the source of deviation of load-displacement curves from Kick's law we observed. The experiments are conducted under quasi-static conditions, thus the high-strain rate effect is not involved. The tip bluntness has been taken into account, and the load-displacement ( $P$ - $h$ ) curve shall follow the modified Kick's law

$$P = C(h + \Delta h)^2 \quad (8)$$

where  $\Delta h$  is the compensation displacement which can be determined by the indenter geometrical analysis,  $\Delta h = R(1/\sin\theta - 1)$  where  $R$  is the tip rounding radius, and  $\theta$  is the half cone angle.

It is found that there is always difference between FEM simulation and experimental load-displacement curves, as shown in Figs. 12(a) and (b). Even when the modified Kick's law is used to fit the experimental load-displacement curves, the exponent is still around 1.85 instead of 2. The simulated curves, however, are fitted to equation (8) perfectly due to the elastic-plastic constitutive model used. From

**Table 5** Drucker-Prager parameters for different grain constituents for 0.84 mm Colorado Mason sand

Sand grain size	Silica	Rock	Metal Oxide
$\sigma_0$ (GPa)	3.3	1.4	4.8
$n$	0.19	0.29	0.2
$\beta$ (°)	40	40	0

dimensionless analysis [59], it is found that the nanoindentation load-displacement curves followed the Kick's law (or equation (8) when tip bluntness is considered) naturally. In order to obtain a simulated load-displacement curves match the experimental curves perfectly, a more sophisticated constitutive model, which shall involve additional length scales, is needed. Constitutive models which take indentation size effect [68, 69] into account are likely appropriate to obtain a better fit between simulation and experiment.

## Conclusions

In order to characterize the granular-level mechanical behavior of sand, nanoindentation is conducted on individual Colorado Mason sand grains to obtain their mechanical properties; specifically, Young's modulus, hardness, fracture toughness, and stress-strain relationship. Six main sizes of sand grains, specifically 0.84 mm, 0.6 mm, 0.42 mm, 0.3 mm, 0.21 mm and 0.15 mm, are used in this study. More than 150 nanoindentation experiments are conducted on each size of sand grain, and 1029 sand grains in total. As expected for a brittle material with initial defects, a wide variation in the granular behavior of sand is observed. Representative values (50 percentile) of Young's modulus ( $P_{50}$ ) for the sand grains is found to be 101.9 GPa, hardness to be 12.7 GPa, and fracture toughness to be  $1.52 \text{ MPa} \cdot \text{m}^{0.5}$ . The minimum Young's modulus and hardness are attained at the median grain size of 0.3 mm. The Young's modulus of silica sand, rock, and metal oxide are 109.8 GPa, 80.3 GPa, and 131.0 GPa, respectively. The hardness of silica sand, rock, and metal oxide are 14.8 GPa, 10.7 GPa, and 10.8 GPa, respectively. The fracture toughness of silica sand, rock, and metal are  $1.58 \text{ MPa} \cdot \text{m}^{0.5}$ ,  $1.53 \text{ MPa} \cdot \text{m}^{0.5}$  and  $2.61 \text{ MPa} \cdot \text{m}^{0.5}$ , respectively. The linearly elastic-plastic hardening plastic stress-strain relationship is used to describe the homogenous and isotropic stress-strain behavior for Colorado Mason sand at the granular level through FEM simulation of the nanoindentation. The Drucker-Prager yield criteria is incorporated and an inverse solving approach is used to determine the stress-strain behavior. The yield strength is found to be in the neighborhood of 3 GPa. The data reported here can be used for mesoscale (granular) simulations of sand in which the individual sand grains would have different properties along with a range of distributions obtained in this study.

**Acknowledgements** The support by ONR MURI grant N00014-11-1-0691, AFOSR FA9550-14-1-0227, NSF CMMI-1661246, ECCS-1307997, and CMMI-1636306 is acknowledged. Lu also thanks the Louis A. Beecherl Jr., Chair for additional support. We thank Dr. Dani Fadda for editing the manuscript.

## References

1. Yamamuro JA, Bopp PA, Lade PV (1996) One-dimensional compression of sands at high pressures. *J Geotech Eng* 122:147–154. [https://doi.org/10.1061/\(ASCE\)0733-9410\(1996\)122:2\(147\)](https://doi.org/10.1061/(ASCE)0733-9410(1996)122:2(147))
2. Russell AR, Khalili N (2004) A bounding surface plasticity model for sands exhibiting particle crushing. *Can Geotech J* 41:1179–1192. <https://doi.org/10.1139/t04-065>
3. Graham J, Alfaro M, Ferris G (2004) Compression and strength of dense sand at high pressures and elevated temperatures. *Can Geotech J* 41:1206–1212. <https://doi.org/10.1139/t04-047>
4. Poorooshasb HB, Holubec I, Sherbourne AN (1967) Yielding and flow of sand in Triaxial compression: parts II and III. *Can Geotech J* 4:376–397. <https://doi.org/10.1139/t67-066>
5. Lade PV, Prubucki MJ (1995) Softening and preshearing effects in sand. *Soils Found* 35:93–104. [https://doi.org/10.3208/sandf.35.4\\_93](https://doi.org/10.3208/sandf.35.4_93)
6. Wang Q, Lade P (2001) Shear banding in true triaxial tests and its effect on failure in sand. *J Eng Mech* 127:754–761. [https://doi.org/10.1061/\(ASCE\)0733-9399\(2001\)127:8\(754\)](https://doi.org/10.1061/(ASCE)0733-9399(2001)127:8(754))
7. Martin BE, Kabir ME, Chen W (2013) Undrained high-pressure and high strain-rate response of dry sand under triaxial loading. *Int J Impact Eng* 54:51–63. <https://doi.org/10.1016/j.ijimpeng.2012.10.008>
8. Luo H, Lu H, Cooper WL, Komanduri R (2011) Effect of mass density on the compressive behavior of dry sand under confinement at high strain rates. *Exp Mech* 51:1499–1510. <https://doi.org/10.1007/s11340-011-9475-2>
9. Luo H, Cooper WL, Lu H (2014) Effect of particle size and moisture on the compressive behavior of dense Eglin sand under confinement at high strain rates. *Int J Impact Eng* 65:40–55. [https://doi.org/10.1007/978-3-319-00771-7\\_46](https://doi.org/10.1007/978-3-319-00771-7_46)
10. Luo H, Du Y, Hu Z, Lu H (2015) High-strain rate compressive behavior of dry Mason sand under confinement. In: Song B, Casem D, Kimberley J (eds) *Dynamic behavior of materials*, vol 1. Conference proceedings of the society for experimental mechanics series. Springer, Cham, pp 381–388. [https://doi.org/10.1007/978-3-319-06995-1\\_46](https://doi.org/10.1007/978-3-319-06995-1_46)
11. Booth AM, Hurley R, Lamb MP, Andrade JE (2014) Force chains as the link between particle and bulk friction angles in granular material. *Geophys Res Lett* 41:1–8. <https://doi.org/10.1002/2014GL061981>. Received
12. Hicher PY, Chang CS, Dano C (2008) Multi-scale modeling of grouted sand behavior. *Int J Solids Struct* 45:4362–4374. <https://doi.org/10.1016/j.ijsolstr.2008.03.024>
13. Borg JP, Vogler TJ (2008) Mesoscale simulations of a dart penetrating sand. *Int J Impact Eng* 35:1435–1440. <https://doi.org/10.1016/j.ijimpeng.2008.07.064>
14. Borja RI, Andrade JE (2006) Critical state plasticity. Part VI: meso-scale finite element simulation of strain localization in discrete granular materials. *Comput Methods Appl Mech Eng* 195:5115–5140. <https://doi.org/10.1016/j.cma.2005.08.020>
15. Andrade JE, Avila CF, Hall SA et al (2011) Multiscale modeling and characterization of granular matter: from grain kinematics to continuum mechanics. *J Mech Phys Solids* 59:237–250. <https://doi.org/10.1016/j.jmps.2010.10.009>
16. Einav I (2007) Breakage mechanics-part II: modelling granular materials. *J Mech Phys Solids* 55:1298–1320. <https://doi.org/10.1016/j.jmps.2006.11.004>
17. Bardenhagen SG, Brackbill JU, Sulsky D (2000) The material-point method for granular materials. *Comput Methods Appl Mech Eng* 187:529–541. [https://doi.org/10.1016/S0045-7825\(99\)00338-2](https://doi.org/10.1016/S0045-7825(99)00338-2)
18. Ren B, Fan H, Bergel GL et al (2014) A peridynamics–SPH coupling approach to simulate soil fragmentation induced by shock waves. *Comput Mech* 55:287–302. <https://doi.org/10.1007/s00466-014-1101-6>
19. Senseney CT, Duan Z, Zhang B, Regueiro RA (2017) Combined spheropolyhedral discrete element (DE)–finite element (FE) computational modeling of vertical plate loading on cohesionless soil. *Acta Geotech* 12:593–603. <https://doi.org/10.1007/s11440-016-0519-8>
20. Lai X, Ren B, Fan H et al (2015) Peridynamics simulations of geomaterial fragmentation by impulse loads. *Int J Numer Anal Methods Geomech* 39:1304–1330. <https://doi.org/10.1002/nag>
21. Fan H, Bergel GL, Li S (2016) A hybrid peridynamics–SPH simulation of soil fragmentation by blast loads of buried explosive. *Int J Impact Eng* 87:14–27. <https://doi.org/10.1016/j.ijimpeng.2015.08.006>
22. Zhang B, Regueiro RA (2015) On large deformation granular strain measures for generating stress – strain relations based upon three-dimensional discrete element simulations. *Int J Solids Struct* 66:151–170. <https://doi.org/10.1016/j.ijsolstr.2015.04.012>
23. Mun W, McCartney J (2015) Compression mechanisms of unsaturated clay under high stresses. *Can Geotech J* 52:1–53. <https://doi.org/10.1139/cgj-2014-0438>
24. Fu P, Dafalias YF (2012) Quantification of large and localized deformation in granular materials. *Int J Solids Struct* 49:1741–1752. <https://doi.org/10.1016/j.ijsolstr.2012.03.006>
25. Liao JJ, Yang M-T, Hsieh H-Y (1991) Direct tensile behavior of a transversely isotropic rock. *Int J Rock Mech & Min Sci* 34:831–849. [https://doi.org/10.1016/S1365-1609\(96\)00065-4](https://doi.org/10.1016/S1365-1609(96)00065-4)
26. Lade PV, Duncan JM (1973) Cubical triaxial tests on cohesionless soil. *J Soil Mech Found Div* 99:793–812
27. Haythornthwaite RM (1997) Simple shear in granular media. *Appl Mech Rev* 50:81–86. <https://doi.org/10.1115/1.3101854>
28. Martin BE, Chen W, Song B, Akers SA (2009) Moisture effects on the high strain-rate behavior of sand. *Mech Mater* 41:786–798. <https://doi.org/10.1016/j.mechmat.2009.01.014>
29. Liu Y, Wang B, Yoshino M et al (2005) Combined numerical simulation and nanoindentation for determining mechanical properties of single crystal copper at mesoscale. *J Mech Phys Solids* 53:2718–2741. <https://doi.org/10.1016/j.jmps.2005.07.003>
30. Lu H, Wang B, Ma J et al (2003) Measurement of creep compliance of solid polymers by nanoindentation. *Mech Time-Dependent Mater* 7:189–207. <https://doi.org/10.1023/B:MTDM.0000007217.07156.9b>
31. Xu T, Yoo JH, Babu S et al (2016) Characterization of the mechanical behavior of SU-8 at microscale by viscoelastic analysis. *J Micromechanics Microengineering* 26:105001. <https://doi.org/10.1088/0960-1317/26/10/105001>
32. Xu T, Du Y, Luo H et al (2017) Measurement of temperature-dependent Young’s modulus at a strain rate for a molding compound by nanoindentation. *Exp Mech* 57:1135–1147. <https://doi.org/10.1007/s11340-016-0205-7>
33. Su C, Herbert EG, Sohn S et al (2013) Measurement of power-law creep parameters by instrumented indentation methods. *J Mech Phys Solids* 61:517–536. <https://doi.org/10.1016/j.jmps.2012.09.009>
34. Du Y, Liu XH, Fu B et al (2017) Creep characterization of solder bumps using nanoindentation. *Mech Time-Dependent Mater* 21:287–305. <https://doi.org/10.1007/s11043-016-9330-z>
35. Oliver WC, Pharr GM (1992) An improved technique for determining hardness and elastic modulus using load and displacement sensing indentation experiments. *J Mater Res* 7:1564–1583. <https://doi.org/10.1557/JMR.1992.1564>
36. Oliver WC, Pharr GM (2004) Measurement of hardness and elastic modulus by instrumented indentation: advances in understanding and refinements to methodology. *J Mater Res* 19:3–20. <https://doi.org/10.1557/jmr.2004.19.1.3>
37. Daphalapurkar NP, Wang F, Fu B et al (2011) Determination of mechanical properties of sand grains by Nanoindentation. *Exp Mech* 51:719–728. <https://doi.org/10.1007/s11340-010-9373-z>



38. Wang F, Fu B, Luo H et al (2014) Characterization of the grain-level mechanical behavior of Eglin sand by Nanoindentation. *Exp Mech* 54:871–884. <https://doi.org/10.1007/s11340-013-9845-z>
39. Regueiro R, Pak R, McCarterney J et al (2014) ONR MURI project on soil blast modeling and simulation. In: Song B, Casem D, Kimberley J. (eds) *Dynamic behavior of materials, vol 1. Conference proceedings of the society for experimental mechanics series*. Springer, Cham, pp 341–353. [https://doi.org/10.1007/978-3-319-00771-7\\_42](https://doi.org/10.1007/978-3-319-00771-7_42)
40. Svoboda JS, Mccartney JS (2014) Shearing rate effects on dense sand and compacted clay. In: Song B, Casem D, Kimberley J (eds) *Dynamic behavior of materials, vol 1. Conference proceedings of the society for experimental mechanics series*. Springer, Cham, pp 389–395. [https://doi.org/10.1007/978-3-319-00771-7\\_47](https://doi.org/10.1007/978-3-319-00771-7_47)
41. Druckrey A, Casem D, Alshibli K, Huskins E (2017) Influence of loading rate on fracture strength of individual sand particles. In: Casem D, Lamberson L, Kimberley J (eds) *Dynamic behavior of materials, vol 1. Conference proceedings of the society for experimental mechanics series*. Springer, Cham, pp 75–80. [https://doi.org/10.1007/978-3-319-41132-3\\_11](https://doi.org/10.1007/978-3-319-41132-3_11)
42. Fan H, Li S (2017) A Peridynamics-SPH modeling and simulation of blast fragmentation of soil under buried explosive loads. *Comput Methods Appl Mech Eng* 318:349–381. <https://doi.org/10.1016/j.cma.2017.01.026>
43. Druckrey AM, Alshibli KA (2016) 3D finite element modeling of sand particle fracture based on in situ X-ray synchrotron imaging. *Int J Numer Anal Methods Geomech* 40:105–116. <https://doi.org/10.1002/nag>
44. Luo H, Hu Z, Xu T, Lu H (2017) High-strain rate compressive behavior of a clay under uniaxial strain state. In: Casem D, Lamberson L, Kimberley J (eds) *Dynamic behavior of materials, vol 1. Conference proceedings of the society for experimental mechanics series*. Springer, Cham, pp 117–122. [https://doi.org/10.1007/978-3-319-41132-3\\_16](https://doi.org/10.1007/978-3-319-41132-3_16)
45. Fan H, Li S (2017) Parallel peridynamics-SPH simulation of explosion induced soil fragmentation by using OpenMP. *Comp Part Mech* 4:199–211. <https://doi.org/10.1007/s40571-016-0116-5>
46. Hansen C, Pak RYS (2016) Centrifuge characterization of buried, explosive-induced soil Ejecta kinematics and crater morphology. *J Dyn Behav Mater* 2:306–325. <https://doi.org/10.1007/s40870-016-0067-1>
47. Hu Z, Du Y, Luo H et al (2014) Internal deformation measurement and force chain characterization of Mason sand under confined compression using incremental digital volume correlation. *Exp Mech* 54:1575–1586. <https://doi.org/10.1007/s11340-014-9915-x>
48. Antis GR, Chantikul P, Lawn BR, Marshall DB (1981) A critical evaluation of Indentation techniques for measuring fracture toughness: I, direct crack measurements. *J Am Ceram Soc* 46:533–538. <https://doi.org/10.1111/j.1151-2916.1981.tb10320.x>
49. Drucker D, Prager W (1952) Soil mechanics and plastic analysis or limit design. *Q Appl Math* 10:157–165
50. Resende L, Martin JB (1985) Formulation of Drucker-Prager cap model. *J Eng Mech* 111:855–881. [https://doi.org/10.1061/\(ASCE\)0733-9399\(1985\)111:7\(855\)](https://doi.org/10.1061/(ASCE)0733-9399(1985)111:7(855))
51. Han LH, Elliott JA, Bentham AC et al (2008) A modified Drucker-Prager cap model for die compaction simulation of pharmaceutical powders. *Int J Solids Struct* 45:3088–3106. <https://doi.org/10.1016/j.ijsolstr.2008.01.024>
52. Cooper WL, Breaux BA (2010) Grain fracture in rapid particulate media deformation and a particulate media research roadmap from the PMEE workshops. *Int J Fract* 162:137–150. <https://doi.org/10.1007/s10704-010-9467-8>
53. Chollacoop N, Dao M, Suresh S (2003) Depth-sensing instrumented indentation with dual sharp indenters. *Acta Mater* 51:3713–3729. [https://doi.org/10.1016/S1359-6454\(03\)00186-1](https://doi.org/10.1016/S1359-6454(03)00186-1)
54. Shim S, il JJ, Pharr GM (2008) Extraction of flow properties of single-crystal silicon carbide by nanoindentation and finite-element simulation. *Acta Mater* 56:3824–3832. <https://doi.org/10.1016/j.actamat.2008.04.013>
55. Peng G, Feng Y, Wen D, Zhang T (2014) An instrumented indentation method for evaluating the effect of hydrostatic pressure on the yield strength of solid polymers. *J Mater Res* 29:2973–2981. <https://doi.org/10.1557/jmr.2014.330>
56. Weibull W (1951) A statistical distribution function of wide applicability. *J Appl Mech* 18:293–297
57. Harding DS, Oliver WC, Pharr GM (1994) Cracking during Nanoindentation and its use in the measurement of fracture toughness. *MRS Proc* 356:663–668. <https://doi.org/10.1557/PROC-356-663>
58. Attaf MT (2004) Connection between the loading curve models in elastoplastic indentation. *Mater Lett* 58:3491–3498. <https://doi.org/10.1016/j.matlet.2004.06.049>
59. Cheng Y, Cheng C (2004) Scaling, dimensional analysis, and indentation measurements. 44:91–149. doi:<https://doi.org/10.1016/j.msar.2004.05.001>
60. Dao M, Chollacoop N, Van Vliet KJ et al (2001) Computational modeling of the forward and reverse problems in instrumented sharp indentation. *Acta Mater* 49:3899–3918. [https://doi.org/10.1016/S1359-6454\(01\)00295-6](https://doi.org/10.1016/S1359-6454(01)00295-6)
61. Chen J, Shi X, Beake BD et al (2016) An investigation into the dynamic indentation response of metallic materials. *J Mater Sci* 51: 8310–8322. <https://doi.org/10.1007/s10853-016-0031-4>
62. Merle B, Maier V, Durst K (2014) Experimental and theoretical confirmation of the scaling exponent 2 in pyramidal load displacement data for depth sensing indentation. *Scanning* 36:526–529. <https://doi.org/10.1002/sca.21151>
63. Cheng C-M, Cheng Y-T (1998) Further analysis of indentation loading curves: effects of tip rounding on mechanical property measurements. *J Mater Res* 13:1059–1064. <https://doi.org/10.1557/JMR.1998.0147>
64. Park J-S, Lee Y-H, Kim Y, Hahn J-H (2012) Prediction of bluntness for pyramidal indenters from nanoindentation curves. *Surf Coatings Technol* 211:148–151. <https://doi.org/10.1016/j.surfcoat.2011.06.059>
65. Kim M, Bang S, Rickhey F, Lee H (2014) Correction of indentation load-depth curve based on elastic deformation of sharp indenter. *Mech Mater* 69:146–158. <https://doi.org/10.1016/j.mechmat.2013.10.002>
66. Nix WD, Gao HJ (1998) Indentation size effects in crystalline materials: a law for strain gradient plasticity. *J Mech Phys Solids* 46: 411–425. [https://doi.org/10.1016/s0022-5096\(97\)00086-0](https://doi.org/10.1016/s0022-5096(97)00086-0)
67. Huang Y, Gao H, Nix WD, Hutchinson JW (2000) Mechanism-based strain gradient plasticity—II. Analysis. *J Mech Phys Solids* 48:99–128. [https://doi.org/10.1016/S0022-5096\(99\)00022-8](https://doi.org/10.1016/S0022-5096(99)00022-8)
68. Huang Y, Zhang F, Hwang KC et al (2006) A model of size effects in nano-indentation. *J Mech Phys Solids* 54:1668–1686. <https://doi.org/10.1016/j.jmps.2006.02.002>
69. Cao YP, Lu J (2005) Size-dependent sharp indentation-I: a closedform expression of the indentation loading curve. *J Mech Phys Solids* 53:33–48. <https://doi.org/10.1016/j.jmps.2004.06.005>
70. Cheng G, Choi KS, Hu X, Sun X (2016) Determining individual phase properties in a multi-phase Q&P steel using multi-scale indentation tests. *Mater Sci Eng A* 652:384–395. <https://doi.org/10.1016/j.msea.2015.11.072>